

# Information Geometry for Landmark Shape Analysis: Unifying Shape Representation and Deformation

Adrian Peter<sup>1</sup> and Anand Rangarajan<sup>2</sup>

<sup>1</sup>Dept. of ECE, <sup>2</sup>Dept. of CISE, University of Florida, Gainesville, FL

**Abstract.** Shape matching plays a prominent role in the comparison of similar structures. We present a unifying framework for shape matching that uses mixture-models to couple both the shape representation and deformation. The theoretical foundation is drawn from information geometry wherein information matrices are used to establish intrinsic distances between parametric densities. When a parameterized probability density function is used to represent a landmark-based shape, the modes of deformation are automatically established through the information matrix of the density. We first show that given two shapes parameterized by Gaussian mixture models, the well known Fisher information matrix of the mixture model is also a Riemannian metric (actually the Fisher-Rao Riemannian metric) and can therefore be used for computing shape geodesics. The Fisher-Rao metric has the advantage of being an intrinsic metric and invariant to reparameterization. The geodesic—computed using this metric—establishes an intrinsic deformation between the shapes, thus unifying both shape representation and deformation. A fundamental drawback of the Fisher-Rao metric is that it is NOT available in closed-form for the Gaussian mixture model. Consequently, shape comparisons are computationally very expensive. To address this, we develop a new Riemannian metric based on generalized  $\phi$ -entropy measures. In sharp contrast to the Fisher-Rao metric, the new metric is available in closed-form. Geodesic computations using the new metric are considerably more efficient. We validate the performance and discriminative capabilities of these new information geometry based metrics by pairwise matching of corpus callosum shapes. A comprehensive comparative analysis is also provided using other landmark based distances, including the Hausdorff distance, the Procrustes metric, landmark based diffeomorphisms, and the bending energies of the thin-plate (TPS) and Wendland splines.

## 1 Introduction

Shape analysis is a key ingredient to many computer vision and medical imaging applications that seek to study the intimate relationship between the form and function of natural, cultural, medical and biological structures. In particular, landmark-based deformable models have been widely used [1] in quantified studies requiring size and shape similarity comparisons. Shape comparison across subjects and modalities require the computation of similarity measures which in turn rely upon non-rigid deformation parameterizations. Almost all of the previous work in this area uses separate models for shape representation and deformation. The principal goal of this paper is to show that shape representations beget shape deformation parameterizations [2,3]. This unexpected unification directly leads to a shape comparison measure.

A brief, cross-cutting survey of existing work in shape analysis illustrates several taxonomies and summaries. Shape deformation parameterizations range from Procrustean metrics [4] to spline-based models [5,6], and from PCA-based modes of deformation [7] to landmark diffeomorphisms [8,9]. Shape representations range from unstructured point-sets [10,11] to weighted graphs [12] and include curves, surfaces and other geometric models [13]. These advances have been instrumental in solidifying the shape analysis landscape. However, one commonality in virtually all of this previous work is the use of separate models for shape representation and deformation.

In this paper, we use probabilistic models for shape representation. Specifically, Gaussian mixture models (GMM) are used to represent unstructured landmarks for a pair of shapes. Since the two density functions are from the same parameterized family of densities, we show how a Riemannian metric arising from their information matrix can be used to construct a geodesic between the shapes. We first discuss the Fisher-Rao metric which is actually the Fisher information matrix of the GMM. To motivate the use of the Fisher-Rao metric, assume for the moment that a deformation applied to a set of landmarks creates a slightly warped set. The new set of landmarks can also be modeled using another mixture model. In the limit of infinitesimal deformations, the Kullback-Leibler (KL) distance between the two densities is a quadratic form with the

Fisher information matrix playing the role of the metric tensor. Using this fact, we can compute a geodesic distance between two mixture models (with the same number of parameters).

A logical question arose out of our investigations with the Fisher information matrix: Are we always handcuffed to the Fisher-Rao Riemannian metric when trying to establish distances between parametric, probabilistic models? (Remember in this context the parametric models are used to represent shapes.) The metric’s close connections to Shannon entropy and the concomitant use of Fisher information in parameter estimation have cemented it as the incumbent information measure. It has also been proliferated by research efforts in information geometry, where one can show its proportionality to popular divergence measures such as Kullback-Leibler. However, the algebraic form of the Fisher-Rao metric tensor makes it very difficult to use when applied to multi-parameter spaces like mixture models. For instance, it is not possible to derive closed-form solutions for the metric tensor or its derivative. To address many of these computational inefficiencies that arise when using the standard information metric, we introduce a new Riemannian metric based on the generalized notion of a  $\phi$ -entropy functional. We take on the challenge of improving the initial Fisher-based model by incorporating the notion of generalized information metrics as first shown by Burbea and Rao [14].

In Section 2, we begin by discussing the probabilistic representation model for landmark shapes. We show how it is possible to go from a landmark representation to one using GMMs. We look at the underlying assumptions and their consequences which play a vital role in interpreting the analysis. Section 3 illustrates the theory and intuition behind how one directly obtains a deformation model from the representation. It provides a brief summary of the necessary information geometry background needed to understand all subsequent analysis. We illustrate connections between the Fisher information and its use as a Riemannian metric to compute a shortest path between two densities. We then motivate generalizations by discussing Burbea and Rao’s work on obtaining differential metrics using the  $\phi$ -entropy functional in parametric probability spaces. The use of a specific  $\phi$ -function leads to an  $\alpha$ -order entropy first introduced by Havrda and Charvát [15]. This can in turn be utilized to develop a new metric ( *$\alpha$ -order entropy metric*) that leads to closed-form solutions for the Christoffel symbols when using a Gaussian mixture models (GMM) for coupling shape representation and deformation. This enables almost an order of magnitude performance increase over the Fisher-Rao based solution. Section 4 validates the Fisher-Rao and  $\alpha$ -order entropy metrics by using them to compute shape distances between corpus callosum data and provides extensive comparative analysis with several other popular landmark-based shape distances.

## 2 The Representation Model: From Landmarks To Mixtures

In this section we motivate the use of probabilistic models, specifically mixture models, for shape representation. Suppose we are given two planar shapes,  $S_1$  and  $S_2$ , consisting of  $K$  landmarks.

$$S_1 = \{\mathbf{u}_1, \mathbf{u}_2, \dots, \mathbf{u}_K\}, S_2 = \{\mathbf{v}_1, \mathbf{v}_2, \dots, \mathbf{v}_K\} \quad (1)$$

where  $\mathbf{u}_a = [u_a^1, u_a^2]^T$ ,  $\mathbf{v}_a = [v_a^1, v_a^2]^T \in \mathbb{R}^2$ ,  $\forall a \in \{1, \dots, K\}$ . Typical shape matching representation models consider the landmarks as a collection of points in  $\mathbb{R}^2$  or as a vector in  $\mathbb{R}^{2K}$ . A consequence with these representations is that if one wishes to perform deformation analysis between the shapes, a separate model needs to be imposed, e.g. thin-plate splines or landmark diffeomorphisms, to establish a map from one shape to the other. (For landmark matching, the correspondence between the shapes is assumed to be known.) In Section 3, we show how the probabilistic shape representation we present here provides an intrinsic warping between the shapes—thus unifying both shape representation and deformation.

Mixture model representations have been used to solve a variety of shape analysis problems, e.g. [16,17]. We select the most frequently used mixture-model to represent our shapes by using a  $K$ -component Gaussian mixture model (GMM) where the shape landmarks are the centers (i.e. the  $a^{\text{th}}$  landmark position serves as the  $a^{\text{th}}$  mean for a specific bi-variate component of the GMM). This parametric, GMM representation for the shapes is given by [18]

$$p(\mathbf{x}|\theta) = \frac{1}{2\pi\sigma^2 K} \sum_{a=1}^K \exp\left\{-\frac{\|\mathbf{x} - \phi_a\|^2}{2\sigma^2}\right\} \quad (2)$$

where  $\theta$  is the set consisting of all landmarks,  $\phi_a = [\theta^{(2a-1)}, \theta^{(2a)}]^T$ ,  $\mathbf{x} = [x^{(1)}, x^{(2)}]^T \in \mathbb{R}^2$  and equal weight priors are assigned to all components, i.e.  $\frac{1}{K}$ . Though we only discuss planar shapes, it is mathematically

straightforward to extend to 3D. The variance  $\sigma^2$  can capture uncertainties that arise in landmark placement and/or natural variability across a population of shapes. Incorporating full component-wise elliptical covariance matrices provides the flexibility to model structurally complicated shapes. The equal weighting on the component-wise priors is acceptable in the absence of any *a priori* knowledge. Figure 1 illustrates this representation model for three different values of  $\sigma^2$ . The input shape consists of 63 landmarks drawn by an expert

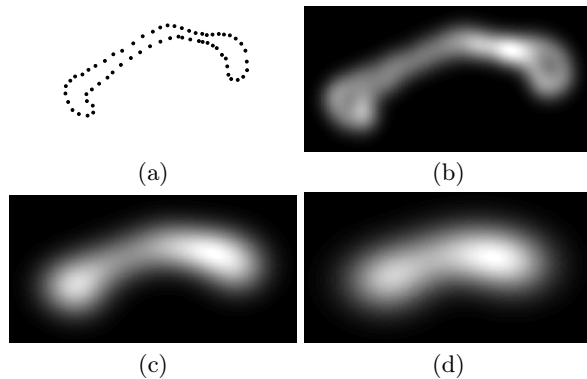


**Fig. 1.** Examples of the probabilistic representation model. (a) Original shape consisting of 63 landmarks ( $K = 63$ ) . (b-d)  $K$ -component GMM using  $\sigma^2 = 0.1$ ,  $\sigma^2 = 0.5$ , and  $\sigma^2 = 1.5$  respectively.

from MRI images of the corpus callosum. The variance is a free parameter in our shape matching algorithm and in practice it is selected to control the size of the neighborhood of influence for nearby landmarks. As evident in the figure, another interpretation is that larger variances blur locations of high curvature present in the corpus callosum curves. Thus, depending on the application we can dial-in the sensitivities to different types of local deformations. Due to these desirable properties, the choice of the variance is currently a free parameter in our algorithm and is isotropic across all components of the GMM. So far we have only focused on the use of GMMs for landmarks. However, they are also well suited for dense point cloud representation of shapes. In such applications, the mean and covariance matrix can be directly estimated from the data via standard parameter estimation techniques.

The real advantage in representing a shape using a parametric density is that it allows us to perform rich geometric analysis on the density’s parameter space. The next section covers how this interpretation in the theoretical setting of information geometry allows us to use the same representation model to deform shapes.

### 3 The Deformation Model: Riemannian Metrics from Information Matrices of Mixtures

We now address the issue of how the same landmark shape representation given by (2) can also be used to enable the computation of deformations between shapes. The overarching idea will be to use the parametric model to calculate the information matrix which is a Riemannian metric on the parameter space of densities. If any two shapes are represented using the same family of parametric densities, the metric tensor will allow us to take a “walk” between them. The next section uses the Fisher-Rao metric to motivate some key ideas from information geometry used in subsequent parts of the paper. We then discuss how to apply the the popular Fisher-Rao metric to shape matching and develop the fully intrinsic deformation framework. Next, we show how it is possible to derive other information matrices starting from the notion of a generalized entropy. The last subsection puts forth a possible solution on how movement of landmarks on the intrinsic space can be used to drive the extrinsic space deformation, a necessity for applying these methods to applications such as shape registration.

### 3.1 The Skinny on Information Geometry

It was Rao [19] who first established that the Fisher information matrix satisfies the properties of a metric on a Riemannian manifold. This is the reasoning behind our nomenclature of *Fisher-Rao* metric whenever the Fisher information matrix is used in this geometric manner. The Fisher information matrix arises from multi-parameter densities, where the  $(i, j)$  entry of the matrix is given by

$$g_{ij}(\theta) = \int p(\mathbf{x}|\theta) \frac{\partial}{\partial \theta^i} \log p(\mathbf{x}|\theta) \frac{\partial}{\partial \theta^j} \log p(\mathbf{x}|\theta) d\mathbf{x}. \quad (3)$$

The Fisher-Rao metric tensor (3) is an intrinsic measure, allowing us to analyze a finite,  $n$ -dimensional statistical manifold  $M$  without considering how  $M$  sits in an  $\mathbb{R}^{n+1}$  space. In this parametric, statistical manifold,  $p \in M$  is a probability density with its local coordinates defined by the model parameters. For example, a bi-variate Gaussian density can be represented as a single point on 4-dimensional manifold with coordinates  $\theta = (\mu^{(1)}, \mu^{(2)}, \sigma^{(1)}, \sigma^{(2)})^T$ , where as usual these represent the mean and standard deviation of the density. (The superscript labeling of coordinates is used to be consistent with differential geometry references.) For the present interest in landmark matching,  $\dim(M) = 2K$  because we only use the means of a GMM as the manifold coordinates for a  $K$  landmark shape. (Recall that  $\sigma$  is a free parameter in the analysis).

The exploitation of the Fisher-Rao metric on statistical manifolds is part of the overarching theory of information geometry [20]. Its utility is largely motivated by Čencov’s theorem [21] which proved that the Fisher-Rao metric is the only metric that is invariant under mappings referred to as congruent embeddings by Markov morphisms. In addition to the invariance property, it can also be shown that many of the other common metrics on probability densities (e.g. Kullback-Leibler, Jensen-Shannon, etc.) can be written in terms of the Fisher-Rao metric given that the densities are close [20]. For example, the Kullback-Leibler (KL) divergence between two parametric densities with parameters  $\theta$  and  $\theta + \delta\theta$  respectively, is proportional to the Fisher-Rao metric  $g$

$$D(p(x|\theta + \delta\theta)||p(x|\theta)) \approx \frac{1}{2}(\delta\theta)^T g \delta\theta. \quad (4)$$

In other words, the Fisher-Rao metric is equal to, within a constant, a quadratic form with the Fisher information playing the role of the Hessian. The use of the information matrix to measure distance between distributions has popularized its use in several applications in computer vision and machine learning. In [22] the authors have used it to provide a more intuitive, geometric explanation of model selection criteria such as the minimum description length (MDL) criterion. To our knowledge, there have been only two other recent uses of the Fisher-Rao metric for computer vision related analyses. The first by Maybank [23], utilizes Fisher information for line detection. The second by Mio *et al.* [24], applies non-parametric Fisher-Rao metrics for image segmentation.

Information geometry incorporates several other differential geometry concepts in the setting of probability distributions and densities. Besides having a metric, we also require the construct of connections to move from one tangent space to another. The connections are facilitated by computing Christoffel symbols of the first kind,  $\Gamma_{k,ij} \stackrel{\text{def}}{=} \frac{1}{2} \left\{ \frac{\partial g_{ik}}{\partial \theta^j} + \frac{\partial g_{kj}}{\partial \theta^i} - \frac{\partial g_{ij}}{\partial \theta^k} \right\}$ , which rely on the partial derivatives of the metric tensor. It is also possible to compute Christoffel symbols of the second kind which involve the inverse of the metric tensor. Since all analysis is intrinsic, i.e. on the surface of the manifold, finding the shortest distance between points on the manifold amounts to finding a geodesic between them. Recall that in the context of shape matching, points on the manifold are parametric densities which in turn represent landmark shapes. Figure 2 illustrates this overall idea. The two shapes are represented using mixture models, the parameters of which map to points on the manifold. The goal is to use the metric tensor to find a geodesic between them. Walking along the geodesic will give us intermediate landmark shapes and the geodesic length will give us an intrinsic shape distance.

### 3.2 Fisher-Rao Metric for Shape Matching

To discover the desired geodesic between two GMM represented landmark shapes (1), we can use the Fisher-Rao metric (3) to formulate a path length between them as

$$s = \int_0^1 g_{ij} \dot{\theta}^i \dot{\theta}^j dt \quad (5)$$

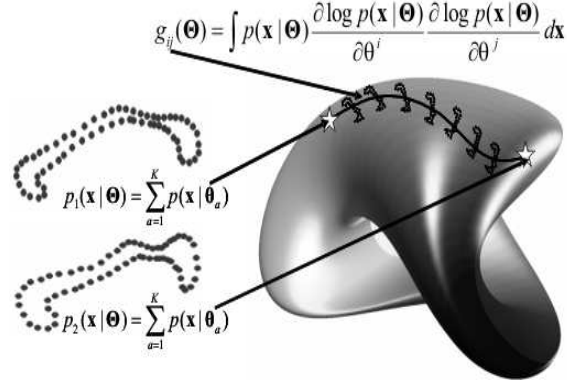


**Fig. 2.** Intrinsic shape matching. Two landmark shapes end up as two points on the manifold. Using the metric tensor  $g_{i,j}$  it is possible to obtain a geodesic between the shapes.

where the standard Einstein summation convention (where summation symbols are dropped) is assumed and  $\dot{\theta}^i = \frac{d\theta^i}{dt}$  is the parameter time derivative. Technically (5) is the square of the geodesic distance, but has the same minimizer as  $\int_0^1 \sqrt{g_{ij} \dot{\theta}^i \dot{\theta}^j} dt$  [25]. Note we have introduced a geodesic curve parameter  $t$  where  $t \in [0, 1]$ . The geodesic path is denoted  $\theta(t)$  and at  $t = 0$  and at  $t = 1$  we have the end points of our path on the manifold, for instance

$$\theta(0) \stackrel{\text{def}}{=} \begin{bmatrix} \theta^{(1)}(0) \\ \theta^{(2)}(0) \\ \theta^{(3)}(0) \\ \theta^{(4)}(0) \\ \vdots \\ \theta^{(2K-1)}(0) \\ \theta^{(2K)}(0) \end{bmatrix} = \begin{bmatrix} u_1^{(1)} \\ u_1^{(2)} \\ u_2^{(1)} \\ u_2^{(2)} \\ \vdots \\ u_K^{(1)} \\ u_K^{(2)} \end{bmatrix}. \quad (6)$$

$\theta(1)$  is defined similarly and as shown they represent the landmarks of the reference and target shape respectively. The functional (5) is minimized using standard calculus of variations techniques leading to the following Euler-Lagrange equations

$$\frac{\delta \mathcal{E}}{\delta \theta^k} = -2g_{ki} \ddot{\theta}^i + \left\{ \frac{\partial g_{ij}}{\partial \theta^k} - \frac{\partial g_{ik}}{\partial \theta^j} - \frac{\partial g_{kj}}{\partial \theta^i} \right\} \dot{\theta}^i \dot{\theta}^j = 0. \quad (7)$$

This can be rewritten in the more standard form

$$g_{ki} \ddot{\theta}^i + \Gamma_{k,ij} \dot{\theta}^i \dot{\theta}^j = 0 \quad (8)$$

This is a system of second order ODEs and not analytically solvable when using GMMs. One can use gradient descent to find a local solution to the system with update equations

$$\theta_{\tau+1}^k(t) = \theta_{\tau}^k(t) - \alpha_{(\tau+1)} \frac{\delta E}{\delta \theta_{\tau}^k(t)}, \forall t \quad (9)$$

where  $\tau$  represents the iteration step and  $\alpha$  the step size. It is worth noting that one can apply other optimization techniques to minimize (5). To this end, in [26], the authors have proposed an elegant technique based on numerical approximations and local eigenvalue analysis of the metric tensor. Their proposed method works well for shapes with a small number of landmarks but the speed of convergence can degrade considerably when the cardinality of the landmarks is large. This due to requirement of repeatedly computing eigenvalues of large matrices. Alternate methods, e.g. quasi-Newton algorithms, can provide accelerated convergence while avoiding expensive matrix manipulations. In the next section we investigate a general class of information matrices which also satisfy the property of being Riemannian metrics. Thus the analysis presented

above to find the geodesic between two shapes holds and simply requires replacing the Fisher-Rao metric tensor by the new  $g_{i,j}$ .

### 3.3 Beyond Fisher-Rao: $\phi$ -Entropy and $\alpha$ -Order Entropy Metrics

Rao's seminal work and the Fisher information matrix's relationship to the Shannon entropy have entrenched it as the metric tensor of choice when trying to establish a distance metric between two parametric models. However, Burbea and Rao went on to show that the notion of distances between parametric models can be extended to a large class of generalized metrics [14]. They defined the generalized  $\phi$ -entropy functional

$$H_\phi(p) = - \int_{\chi} \phi(p) d\mathbf{x} \quad (10)$$

where  $\chi$  is the measurable space (for our purposes  $\mathbb{R}^2$ ), and  $\phi$  is a  $C^2$ -convex function defined on  $\mathbb{R}_+ \equiv [0, \infty)$ . (For readability we will regularly replace  $p(\mathbf{x}|\theta)$  with  $p$ .) The metric on the parameter space is obtained by finding the Hessian of (10) along a direction in its tangent space. Assuming sufficient regularity properties on  $\theta = \{\theta^1, \dots, \theta^n\}$ , the direction can be obtained by taking the total differential of  $p(\mathbf{x}|\theta)$  w.r.t  $\theta$

$$dp(\theta) = \sum_{k=1}^n \frac{\partial p}{\partial \theta^k} d\theta^k . \quad (11)$$

This results in the Hessian being defined as

$$\Delta_\theta H_\phi(p) = - \int_{\chi} \phi''(p) [dp(\theta)]^2 d\mathbf{x} \quad (12)$$

and directly leads to the following differential metric satisfying Riemannian metric properties

$$ds_\phi^2(\theta) = -\Delta_\theta H_\phi(p) = \sum_{i,j=1}^n g_{i,j}^\phi d\theta^i d\theta^j , \quad (13)$$

where

$$g_{i,j}^\phi = \int_{\chi} \phi''(p) \left(\frac{\partial p}{\partial \theta^i}\right) \left(\frac{\partial p}{\partial \theta^j}\right) d\mathbf{x} . \quad (14)$$

The metric tensor in (14) is called the  $\phi$ -entropy matrix. By letting

$$\phi(p) = p \log p, \quad (15)$$

equation (10) becomes the familiar Shannon entropy and (14) yields the Fisher information matrix. One major drawback of using the Fisher-Rao metric is that the computation of geodesics is very inefficient as they require numerical calculation of the integral in (3).

We now discuss an alternative choice of  $\phi$  that directly leads to a new Riemannian metric and enables us to derive closed-form solutions for (14). Our desire to find a computationally efficient information metric was motivated by noticing that if the integral of the metric could be reduced to just a correlation between the partials of the density w.r.t  $\theta^i$  and  $\theta^j$ , i.e.  $\int \frac{\partial p}{\partial \theta^i} \frac{\partial p}{\partial \theta^j} d\mathbf{x}$ , then the GMM would reduce to separable one dimensional Gaussian integrals for which the closed-form solution exists. In the framework of generalized  $\phi$ -entropies, this idea translated to selecting a  $\phi$  such that  $\phi''$  becomes a constant in (14). In [15], Havrda and Charvát introduced the notion of a  $\alpha$ -order entropy using the convex function

$$\phi(p) = (\alpha - 1)^{-1} (p^\alpha - p), \quad \alpha \neq 1 . \quad (16)$$

As  $\lim_{\alpha \rightarrow 1} \phi(p)$ , (16) tends to (15). To obtain our desired form, we set  $\alpha = 2$  which results in  $\frac{1}{2}\phi'' = 1$ . (The one-half scaling factor does not impact the metric properties.) Thus, the new metric is defined as

$$g_{i,j}^\alpha = \int_{\chi} \left(\frac{\partial p}{\partial \theta^i}\right) \left(\frac{\partial p}{\partial \theta^j}\right) d\mathbf{x} \quad (17)$$

and we refer to it as the  $\alpha$ -order entropy metric tensor. The reader is referred to the Appendix in [3] where we provide some closed-form solutions to the  $\alpha$ -order entropy metric tensor and the necessary derivative calculations needed to compute (17). Though we were computationally motivated in deriving this metric, it will be shown via experimental results that it has shape discriminability properties similar to that of the Fisher-Rao and other shape distances. Deriving the new metric also opens the door for further research into applications of the metric to other engineering solutions. Under this generalized framework, there are opportunities to discover other application-specific information matrices that retain Riemannian metric properties.

### 3.4 Extrinsic Deformation

The previous sections illustrated the derivations of the probabilistic Riemannian metrics which led to a completely intrinsic model for establishing the geodesic between two landmark shapes on a statistical manifold. Once the geodesic has been found, traversing this path yields a new set of  $\theta$ 's at each discretized location of  $t$  which in turn represents an intermediate, intrinsically deformed landmark shape. We would also like to use the results of our intrinsic model to go back and warp the extrinsic space.

Notice that the intrinsic deformation of the landmarks only required our  $\theta$ 's to be parametrized by time. Deformation of the ambient space  $\mathbf{x} \in \mathbb{R}^2$ , i.e. our shape points, can be accomplished via a straightforward incorporation of the time parameter on to our extrinsic space, i.e.

$$p(\mathbf{x}(t)|\theta(t)) = \frac{1}{K} \sum_{a=1}^K \frac{1}{2\pi\sigma^2} \exp\left\{-\frac{1}{2\sigma^2} \|\mathbf{x}(t) - \phi_a(t)\|^2\right\}. \quad (18)$$

We want to deform the  $\mathbf{x}(t)$ 's of extrinsic space through the velocities induced by the intrinsic geodesic and simultaneously preserve the likelihood of all these ambient points relative to our intrinsic  $\theta$ 's. Instead of enforcing this condition on  $L = p(\mathbf{x}(t)|\theta(t))$ , we use the negative log-likelihood  $-\log L$  of the mixture and set the total derivative with respect to the time parameter to zero:

$$\begin{aligned} \frac{d \log L}{dt} &= (\nabla_{\theta^1} \log L)^T \dot{\theta}^1 + (\nabla_{\theta^2} \log L)^T \dot{\theta}^2 \\ &+ \frac{\partial \log L}{\partial x^1(t)} u - \frac{\partial \log L}{\partial x^2(t)} v = 0 \end{aligned} \quad (19)$$

where  $u(t) = \frac{dx^1}{dt}$  and  $v(t) = \frac{dx^2}{dt}$  represent the probabilistic flow field induced by our parametric model. Note that this formulation is analogous to the one we find in optical flow problems. Similar to optical flow, we introduce a thin-plate spline regularizer to smooth the flow field

$$\int (\nabla^2 u)^2 + (\nabla^2 v)^2 d\mathbf{x}. \quad (20)$$

We note that is also possible to use the quadratic variation instead of the Laplacian as the regularizer. On the interior of the grid, both of these satisfy the same biharmonic but the quadratic variation yields smoother flows near the boundaries.

The overall extrinsic space deformation can be modeled using the following energy functional

$$E(u, v) = \int \left( \lambda [(\nabla^2 u)^2 + (\nabla^2 v)^2] + \left[ \frac{d \log L}{dt} \right]^2 \right) d\mathbf{x} \quad (21)$$

where  $\lambda$  is a regularization parameter that weighs the error in the extrinsic motion relative to the departure from smoothness. The minimal flow fields are obtained via the Euler-Lagrange equation of (21). As formulated, the mapping found through the thin-plate regularizer is not guaranteed to be diffeomorphic. This can be enforced if necessary and is currently under investigation for future work. In this section, we have shown that selecting the representation model (18) immediately gave the likelihood preserving data term used to drive the warping of extrinsic shape points thus continuing our theme of unified shape representation and deformation.

## 4 Experimental Results and Analysis

Even though we cannot visualize the abstract statistical manifold induced by our two metrics, we have found it helpful to study the resulting geodesics of basic transformations on simple shapes (Figures 3 and 5). In all figures, the dashed, straight line represents the initialization path and the solid bell-shaped curve shows the final geodesic between shapes. Figure 3 shows a straight-line shape consisting of 21 landmarks that has been slightly collapsed like a hinge. Notice that the resulting geodesic is bent indicating the curved nature of

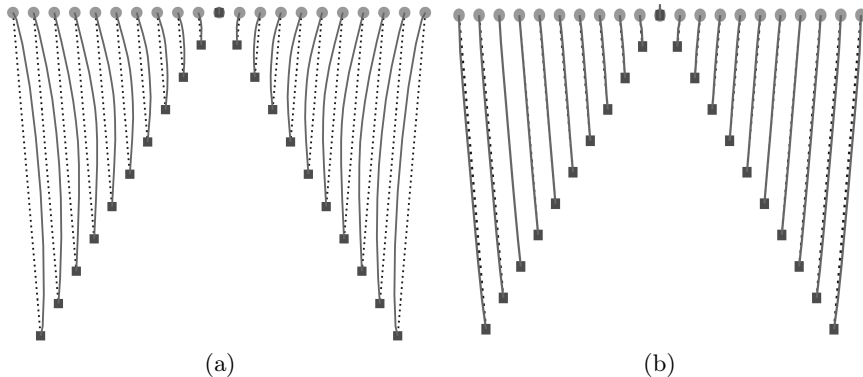


**Fig. 3.** Bending of straight line with 21 landmarks. The dashed line is the initialization and the solid line the final geodesic. (a) Curvature of space under Fisher information metric evident in final geodesic. (b) The space under  $\alpha$ -order entropy metric is not as visually curved for this transformation.

the statistical manifolds. Even though the bending in Figure 3(b) is not as visually obvious, a closer look at the landmark trajectories for a couple of the shape’s landmarks (Figure 4) illustrates how the intermediate landmark positions have re-positioned themselves from their uniform initialization. It is the velocity field

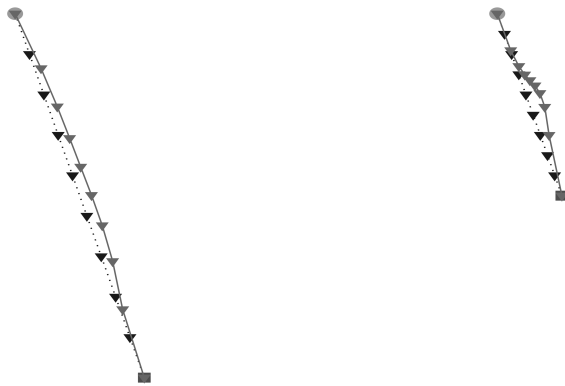


**Fig. 4.** Intermediate landmark trajectories under the  $\alpha$ -order entropy metric tensor. These are the second and third landmarks from the middle in Figure 3(b). The trajectories show that even though the final geodesic looks similar to the straight line initialization, the intermediate landmark positions have changed which results in different velocities along the geodesic.

resulting from these intermediate landmarks that enables a smooth mapping from one shape to another [11]. Figure 5 illustrates geodesics obtained from matching a four-landmark square to one that has been rotated  $210^\circ$  clockwise. The geodesics obtained by the Fisher-Rao metric are again smoothly curved, illustrating the hyperbolic nature of the manifold induced by the information matrix [27] whereas the  $\alpha$ -order entropy

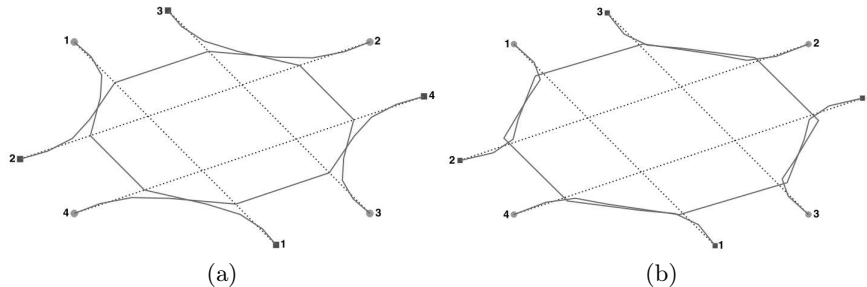


**Fig. 5.** Rotation of square represented with four landmarks. The dashed line is the initialization and the solid line the final geodesic. The circular landmarks are the starting shape and square landmarks the rotated shape. (a) Fisher information metric path is curved smoothly. (b)  $\alpha$ -entropy metric path has sharp corners.

metric displays sharper, abrupt variations. In both cases, we obtained well-behaved geodesics with curved geometry.

For applications in medical imaging, we have evaluated both the Fisher-Rao and  $\alpha$ -order entropy metrics on real data consisting of nine corpora callosa with 63-landmarks each as shown in Figure 6. These landmarks

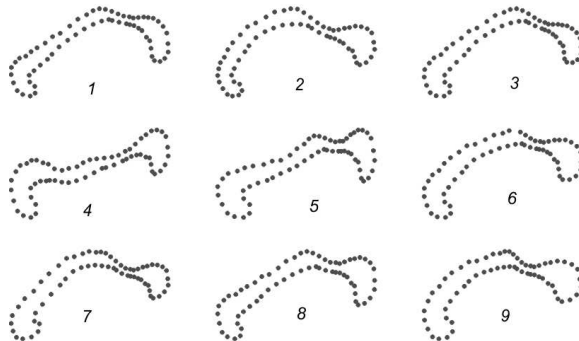


**Fig. 6.** Nine corpus callosum shapes used for pairwise matching, 63 landmarks per shape.

were acquired via manual marking by an expert from different MRI scans. As with all landmark matching algorithms, correspondence between shapes is known. We performed pairwise matching of all shapes in order to study the discriminating capabilities of the metrics. Since both the Fisher-Rao and  $\alpha$ -order entropy metric are obtained from GMMs, we tested both metrics with three different values of the free parameter  $\sigma^2$ . In addition to the two proposed metrics, we performed comparative analysis with several other standard landmark distances and similarity measures. The distance metrics included are Procrustes [4,28], symmetrized Hausdorff [29] and landmark diffeomorphisms [8]. The first two distance metrics have established themselves as a staple for shape comparison while the third is a fairly recent technique with the metric arising from the minimum energy of fitting iterated splines to the infinitesimal velocity vectors that diffeomorphically take one shape onto the other. It is worth noting that in [8], the authors implemented a discrete approximation to their proposed energy functional. In order to minimize any numerical approximation issues and experimental variability, our implementation obtains a gradient descent solution directly on the analytic Euler-Lagrange equations for their functional. The shape similarity measures (which are not metrics) incorporated in the study use the bending energy of spline-based models to map the source landmarks to the target. We used two spline models: the ubiquitous thin-plate spline (TPS) [5] which has basis functions of infinite support and the more recently introduced Wendland spline [30] which has compactly supported bases. For the sake of brevity, we will refer to all measures as metrics or distances with the understanding that the bending energies do not satisfy the required properties of a true metric.

The results of pairwise matching of all nine shapes is listed in Table 1, containing the actual pairwise distances, and Table 2, which lists the ranked matches from best to worst for each metric. Table 2 clearly

shows a global trend in the rankings among the different metrics. For example, almost all the metrics rank pair (4,7) as the worst match. The single discrepancy comes from the Hausdorff metric. However, it lists (4,7) as the penultimately worst match which globally we can take as an agreement in general with the others. This global similarity also holds for the shapes that were most alike which can be seen from the first three rows. One can interpret this agreement in the global sense as a reflection of obvious similarities or dissimilarities among the shapes.

The interesting properties unique to each of these metrics arise in the differences that are apparent in the local trend. We attribute a majority of these local rank differences due to the inherent sensitivities of each metric. These sensitivities are a direct consequences of how they are formulated. For example, it is well known that the Hausdorff metric is biased to outliers due to the *max* – *min* operations in its definition. The bending energy of the spline models is invariant to affine transformations between shapes and its increase is a reflection of how one shape has to be “bent” to the other. The differences among the spline models can be attributed to the compact (Wendland) versus infinite (TPS) support of the basis functions. We refer the reader to the aforementioned references for more through discussions on the respective metrics and their formulations.

Though we are in the early stages of investigating the two new metrics and their properties, these results clearly validate their use as a shape metric. The choice of  $\sigma^2 = \{0.1, 0.5, 1.5\}$  impacted the local rankings among the two metrics. As Figure 1 illustrated,  $\sigma^2$  gives us the ability to “dial-in” the local curvature shape features. When matching shapes, selecting a large value of  $\sigma^2$  implies that we do not want the matching influenced by localized, high curvature points on the shape. Similarly, a low value of  $\sigma^2$  reflects our desire to incorporate such features. As a illustration of this, rows two and three under the Fisher-Rao metric (Table 2) show that for  $\sigma^2 = \{0.1, 0.5\}$ , shape pair (6,8) was ranked as the second best match and pair (3,6) was third. When we set  $\sigma^2 = 1.5$ , pair (3,6) moved to second and (6,8) moved down to third. Hence, we see  $\sigma^2$  impacts the shape distance. However, it affects it in such a way that is discernibly natural – meaning that the ranking was not drastically changed which would not coincide with our visual intuition. The differences between Fisher-Rao and  $\alpha$ -order entropy metric arise from the structural differences in their respective metric tensors  $g_{i,j}$ . The off-diagonal components (corresponding to intra-landmarks) of the  $\alpha$ -order entropy metric tensor are zero. This decouples the correlation between a landmark’s own  $x$ - and  $y$ -coordinates, though correlations exist with the coordinates of other landmarks. Intuitively this changes the curvature of the manifold and shows up visually in the shape of the geodesic [3] which in turn impacts the distance measure.

The  $\alpha$ -order entropy metric provided huge computational benefits over the Fisher-Rao metric. The Fisher-Rao metric requires an extra  $O(N^2)$  computation of the integral over  $\mathbb{R}^2$  where we have assumed an  $N$  point discretization of the  $x$ - and  $y$ -axes. This computation must be repeated at each point along the evolving geodesic and for every *pair* of landmarks. The derivatives of the metric tensor which are needed for geodesic computation require the same  $O(N^2)$  computation for every landmark *triple* and at each point on the evolving geodesic. Since our new  $\phi$ -entropy metric tensor and derivatives are in closed-form, this extra  $O(N^2)$  computation is not required. Please note that the situation only worsens in 3D where  $O(N^3)$  computations will be required for the Fisher-Rao metric (and derivatives) while our new metric (and derivatives) remain in closed-form. It remains to be seen if other closed-form information metrics can be derived which are meaningful in the shape matching context.

The comparative analysis with other metrics illustrated the utility of Fisher-Rao and  $\alpha$ -order entropy metrics as viable shape distance measures. In addition to their discriminating capabilities, these two metrics have several other advantages over the present contemporaries. The representation model based on densities is inherently more robust to noise and uncertainties in the landmark positions. Though we have shown results on shapes that exhibit closed-contour topology, it is worth noting that this formulation has no inherent topological constraints on shape structure—thus enabling landmark analysis for anatomical forms with interior points or disjoint parts. Most importantly, the deformation is directly obtained from the shape representation, eliminating an arbitrary spline term found in some formulations. The robustness and flexibility of this model, has good potential for computational medical applications such as computer-aided diagnosis and biological growth analysis. As a general shape similarity measure, our metrics are yet another tool for general shape recognition problems.

## 5 Conclusions

In this paper, we have presented a unified framework for shape representation and deformation. Previous approaches treat representation and deformation as two distinct problems. Our representation of landmark shapes using mixture models enables immediate application of information matrices as Riemannian metric tensors to establish an intrinsic geodesic between shape pairs. To this end, we discussed two such metrics: the Fisher-Rao metric and the new  $\alpha$ -order entropy metric. To our knowledge, this is the first time these information geometric principles have been applied to shape analysis. In our framework, shapes modeled as densities live on a statistical manifold and intrinsic distances between them are readily obtained by computing the geodesic connecting two shapes. Our development of the  $\alpha$ -order entropy was primarily motivated by the computational burdens of working with the Fisher-Rao metric. Given that our parameter space comes from Gaussian mixture models, the Fisher-Rao metric suffers serious computational inefficiencies as it is not possible to get closed-form solutions to the metric tensor or the Christoffel symbols. The new  $\alpha$ -order entropy metric, with  $\alpha = 2$ , enables us to obtain closed-form solutions to the metric tensor and its derivatives and therefore alleviates this computational burden. We also illustrated how to leverage the intrinsic geodesic path from the two metrics to deform the extrinsic space, important to applications such as registration. Our techniques were applied to matching corpus callosum landmark shapes, illustrating the usefulness of this framework for shape discrimination and deformation analysis. Test results show the applicability of the new metrics to shape matching, providing discriminability similar to several other metrics. Admittedly we are still in the early stages of working with these metrics and have yet to perform statistical comparisons on the computed shape geodesic distances. These metrics also do not suffer from topological constraints on the shape structure (thus enabling their applicability to a large class of image analysis and other shape analysis applications).

Our intrinsic, coupled representation and deformation framework is not only limited to landmark shape analysis where correspondence is assumed to be known. The ultimate practicality and utility of this approach will be realized upon extension of these techniques to unlabeled point sets where correspondence is unknown. Existing solutions to this more difficult problem have only been formulated via models that decouple the shape representation and deformation, e.g. [10]. Though the metrics presented in this work result from second order analysis of the generalized entropy, it is possible to extend the framework to incorporate other probabilistic, Riemannian metrics.

The immediate next step is to move beyond landmarks and model shape point-sets using Gaussian mixture models thereby estimating the free parameter  $\sigma^2$  directly from the data. Our future work will focus on extending this framework to incorporate diffeomorphic warping of the extrinsic space and investigation into other information metrics. Extensions to 3D shape matching are also possible.

## Acknowledgments

This work is partially supported by NSF IIS-0307712 and NIH R01NS046812. We acknowledge helpful conversations with Hongyu Guo, Karl Rohr, Chris Small, and Gnana Bhaskar Tenali.

## References

1. F. L. Bookstein, *Morphometric tools for landmark data: Geometry and biology*. Cambridge University Press, 1991.
2. A. Peter and A. Rangarajan, "Shape matching using the Fisher-Rao Riemannian metric: Unifying shape representation and deformation," *International Symposium on Biomedical Imaging (ISBI)*, pp. 1164–1167, 2006.
3. —, "A new closed-form information metric for shape analysis," in *Medical Image Computing and Computer Assisted Intervention (MICCAI)*, 2006, pp. 249–256.
4. C. Small, *The statistical theory of shape*. New York, NY: Springer, 1996.
5. F. L. Bookstein, "Principal warps: Thin-plate splines and the decomposition of deformations," *IEEE Trans. Patt. Anal. Mach. Intell.*, vol. 11, no. 6, pp. 567–585, June 1989.
6. K. Rohr, H. Stiehl, R. Sprengel, T. Buzug, J. Weese, and M. Kuhn, "Landmark-based elastic registration using approximating thin-plate splines," *IEEE Trans. on Medical Imaging*, vol. 20, no. 6, pp. 526–534, June 2001.
7. R. Davies, C. Twining, T. Cootes, and C. Taylor, "An information theoretic approach to statistical shape modelling," in *European Conference on Computer Vision (ECCV)*. Lecture Notes in Computer Science, Springer, 2002, pp. 3–20.
8. V. Camion and L. Younes, "Geodesic interpolating splines," in *Energy Minimization Methods for Computer Vision and Pattern Recognition (EMMCVPR)*. New York: Springer, 2001, pp. 513–527.
9. S. Joshi and M. Miller, "Landmark matching via large deformation diffeomorphisms," *IEEE Trans. Image Processing*, vol. 9, pp. 1357–1370, 2000.
10. H. Chui and A. Rangarajan, "A new point matching algorithm for non-rigid registration," *Computer Vision and Image Understanding*, vol. 89, pp. 114–141, 2003.
11. H. Guo, A. Rangarajan, and S. Joshi, "Diffeomorphic point matching," in *The Handbook of Mathematical Models in Computer Vision*, N. Paragios, Y. Chen, and O. Faugeras, Eds. Springer Verlag, 2005, pp. 205–220.
12. K. Siddiqi, A. Shokoufandeh, S. J. Dickinson, and S. W. Zucker, "Shock graphs and shape matching," in *International Conference on Computer Vision (ICCV)*, 1998, pp. 222–229.
13. A. Srivastava, S. Joshi, W. Mio, and X. Liu, "Statistical shape analysis: Clustering, learning and testing," *IEEE Transactions on Pattern Analysis and Machine Intelligence*, vol. 27, no. 4, pp. 590–602, 2003.
14. J. Burbea and R. Rao, "Entropy differential metric, distance and divergence measures in probability spaces: A unified approach," *Journal of Multivariate Analysis*, vol. 12, pp. 575–596, 1982.
15. M. E. Havrda and F. Charvát, "Quantification method of classification processes: Concept of structural  $\alpha$ -entropy," *Kybernetika*, vol. 3, pp. 30–35, 1967.
16. F. Wang, B. Vemuri, A. Rangarajan, I. Schmalfluss, and S. Eisenschenk, "Simultaneous nonrigid registration of multiple point sets and atlas construction," in *European Conference on Computer Vision (ECCV)*, 2006, pp. 551–563.
17. T. Cootes and C. Taylor, "A mixture model for representing shape variation," in *Proceedings of British Machine Vision Conference*, 1997, pp. 110–119.
18. G. J. McLachlan and K. E. Basford, *Mixture models: inference and applications to clustering*. New York: Marcel Dekker, 1988.
19. C. Rao, "Information and accuracy attainable in estimation of statistical parameters," *Bulletin of the Calcutta Mathematical Society*, vol. 37, pp. 81–91, 1945.
20. S.-I. Amari and H. Nagaoka, *Methods of Information Geometry*. American Mathematical Society, 2001.
21. N. Čencov, *Statistical decision rules and optimal inference*. American Mathematical Society, 1982.
22. I. J. Myung, V. Balasubramanian, and M. A. Pitt, "Counting probability distributions: Differential geometry and model selection," *Proceedings of the National Academy of Sciences*, vol. 97, pp. 11 170–11 175, 2000.
23. S. Maybank, "The Fisher-Rao metric for projective transformations of the line," *International Journal of Computer Vision*, vol. 63, no. 3, pp. 191–206, 2005.
24. W. Mio, D. Badlyans, and X. Liu, "A computational approach to Fisher information geometry with applications to image analysis," in *Energy Minimization Methods in Computer Vision and Pattern Recognition (EMMCVPR)*, 2005, pp. 18–33.
25. R. Courant and D. Hilbert, *Methods of Mathematical Physics*. Wiley-Interscience, 1989.
26. W. Mio and X. Liu, "Landmark representation of shapes and Fisher-Rao geometry," in *IEEE International Conference on Image Processing*, 2006, pp. 2113–2116.
27. S. Costa, S. Santos, and J. Strapasson, "Fisher information matrix and hyperbolic geometry," *IEEE Information Theory Workshop*, pp. 28–30, 2005.
28. D. G. Kendall, "Shape-manifolds, Procrustean metrics and complex projective spaces," *Bulletin of the London Mathematical Society*, vol. 16, pp. 81–121, 1984.
29. D. P. Huttenlocher, G. A. Klanderman, and W. J. Rucklidge, "Comparing images using the Hausdorff distance," *IEEE Trans. Patt. Anal. Mach. Intell.*, vol. 15, no. 9, pp. 850–863, Sep. 1993.
30. M. Fornefett, K. Rohr, and H. Stiehl, "Radial basis functions with compact support for elastic registration of medical images," *Image and Vision Computing*, vol. 19, no. 1, pp. 87–96, January 2001.

Pairs	Fisher-Rao ( $10^{-2}$ )			$\alpha$ -Order Entropy ( $10^{-3}$ )			Diffeomorphism( $10^{-2}$ )	Procrustes( $10^{-2}$ )	Hausdorff( $10^{-2}$ )	Wendland( $10^{-2}$ )	TPS( $10^{-2}$ )
	$\sigma^2 = .1$	$\sigma^2 = .5$	$\sigma^2 = 1.5$	$\sigma^2 = .1$	$\sigma^2 = .5$	$\sigma^2 = 1.5$					
1 vs. 2	142.25	27.17	5.85	4.67	4.64	0.54	45.05	11.73	27.15	128.39	7.72
1 vs. 3	62.22	14.59	3.80	2.06	2.66	0.40	17.72	7.74	11.83	45.08	1.47
1 vs. 4	375.07	87.04	20.31	13.73	16.29	2.27	114.17	18.95	50.29	203.60	10.60
1 vs. 5	119.75	26.72	6.79	4.09	5.07	0.80	42.80	11.49	25.52	131.52	8.28
1 vs. 6	54.15	9.83	2.02	2.15	2.22	0.26	17.97	7.19	13.85	65.04	4.77
1 vs. 7	206.41	52.81	14.76	7.63	10.96	1.88	81.49	16.53	57.06	227.29	13.28
1 vs. 8	24.07	3.08	0.53	1.05	0.62	0.06	8.20	4.73	5.69	50.89	3.05
1 vs. 9	161.57	32.19	7.36	6.65	8.05	1.07	58.49	13.27	26.54	192.29	12.92
2 vs. 3	106.46	20.92	5.86	3.65	3.82	0.65	39.63	11.21	17.32	123.01	6.48
2 vs. 4	571.37	136.56	29.39	19.65	23.83	3.02	182.93	23.54	117.74	351.38	17.62
2 vs. 5	367.50	86.10	21.29	11.00	14.41	2.16	123.99	19.72	72.76	312.08	16.74
2 vs. 6	73.74	15.88	4.44	2.52	3.24	0.55	34.84	10.31	15.19	110.61	5.55
2 vs. 7	150.02	44.22	15.18	5.03	8.86	1.96	80.38	16.47	71.46	254.76	11.72
2 vs. 8	136.85	27.96	6.39	3.95	4.56	0.60	53.75	12.68	23.35	169.20	9.42
2 vs. 9	94.52	20.60	5.02	3.74	5.59	0.87	43.67	11.53	28.81	147.21	10.52
3 vs. 4	610.51	153.60	38.20	21.85	28.07	4.27	201.91	25.17	93.71	348.10	11.13
3 vs. 5	231.03	53.58	12.41	6.92	8.57	1.12	67.43	14.55	33.53	153.21	6.80
3 vs. 6	34.58	6.21	1.18	1.28	1.16	0.11	9.54	5.17	7.41	28.71	2.74
3 vs. 7	92.02	21.34	5.44	3.67	4.68	0.75	39.61	11.28	19.74	100.58	6.74
3 vs. 8	59.26	13.33	3.27	1.86	2.24	0.32	18.32	7.69	12.11	47.59	2.06
3 vs. 9	119.42	22.62	4.71	5.18	5.75	0.69	40.40	10.96	29.79	116.41	9.39
4 vs. 5	208.30	59.56	19.19	7.54	13.18	2.70	92.67	17.85	32.92	200.05	12.84
4 vs. 6	435.13	110.01	27.50	15.85	21.45	3.32	147.27	21.96	64.50	311.83	23.36
4 vs. 7	682.10	193.47	54.20	25.14	37.77	6.59	229.74	28.60	104.18	499.73	34.32
4 vs. 8	325.84	79.77	19.83	11.48	14.97	2.30	105.93	18.71	61.59	224.42	16.66
4 vs. 9	512.94	132.76	33.98	18.76	26.97	4.17	172.52	23.82	72.78	374.71	25.14
5 vs. 6	163.69	37.42	8.72	4.56	5.68	0.76	56.41	13.01	28.47	157.91	10.74
5 vs. 7	311.52	78.63	19.60	8.88	12.34	1.79	91.71	17.46	74.11	233.17	13.85
5 vs. 8	86.32	20.26	5.17	2.58	3.50	0.56	31.57	9.99	20.78	89.38	4.07
5 vs. 9	270.52	63.21	16.13	7.75	11.11	1.63	81.30	16.31	42.61	224.62	12.78
6 vs. 7	82.06	22.30	6.80	2.58	4.06	0.79	38.31	11.13	23.74	105.01	5.70
6 vs. 8	28.72	5.96	1.21	0.86	1.14	0.14	13.81	6.22	7.76	40.29	3.33
6 vs. 9	43.65	10.11	2.71	1.90	2.80	0.44	21.81	8.04	12.75	59.11	4.05
7 vs. 8	145.55	40.08	11.83	4.62	7.85	1.45	67.70	14.50	38.37	151.59	6.87
7 vs. 9	85.01	21.31	6.45	2.62	3.98	0.70	31.97	10.11	28.22	95.40	5.19
8 vs. 9	103.71	23.95	5.87	3.68	5.62	0.80	47.65	11.84	20.90	126.93	9.24

Table 1. Pairwise shape distances.

Fisher-Rao ( $10^{-2}$ )			$\alpha$ -Order Entropy ( $10^{-3}$ )			Diffeomorphism( $10^{-2}$ )	Procrustes( $10^{-2}$ )	Hausdorff( $10^{-2}$ )	Wendland( $10^{-2}$ )	TPS( $10^{-2}$ )
$\sigma^2 = .1$	$\sigma^2 = .5$	$\sigma^2 = 1.5$	$\sigma^2 = .1$	$\sigma^2 = .5$	$\sigma^2 = 1.5$					
1 vs. 8	1 vs. 8	1 vs. 8	6 vs. 8	1 vs. 8	1 vs. 8	1 vs. 8	1 vs. 8	1 vs. 8	3 vs. 6	1 vs. 3
6 vs. 8	6 vs. 8	3 vs. 6	1 vs. 8	6 vs. 8	3 vs. 6	3 vs. 6	3 vs. 6	3 vs. 6	6 vs. 8	3 vs. 8
3 vs. 6	3 vs. 6	6 vs. 8	3 vs. 6	3 vs. 6	6 vs. 8	6 vs. 8	6 vs. 8	6 vs. 8	1 vs. 3	3 vs. 6
6 vs. 9	1 vs. 6	1 vs. 6	3 vs. 8	1 vs. 6	1 vs. 6	1 vs. 3	1 vs. 6	1 vs. 3	3 vs. 8	1 vs. 8
1 vs. 6	6 vs. 9	6 vs. 9	6 vs. 9	3 vs. 8	3 vs. 8	1 vs. 6	3 vs. 8	3 vs. 8	1 vs. 8	6 vs. 8
3 vs. 8	3 vs. 8	3 vs. 8	1 vs. 3	1 vs. 3	1 vs. 3	3 vs. 8	1 vs. 3	6 vs. 9	6 vs. 9	6 vs. 9
1 vs. 3	1 vs. 3	1 vs. 3	1 vs. 6	6 vs. 9	6 vs. 9	6 vs. 9	6 vs. 9	1 vs. 6	1 vs. 6	5 vs. 8
2 vs. 6	2 vs. 6	2 vs. 6	2 vs. 6	2 vs. 6	1 vs. 2	5 vs. 8	5 vs. 8	2 vs. 6	5 vs. 8	1 vs. 6
6 vs. 7	5 vs. 8	3 vs. 9	5 vs. 8	5 vs. 8	2 vs. 6	7 vs. 9	7 vs. 9	2 vs. 3	7 vs. 9	7 vs. 9
7 vs. 9	2 vs. 9	2 vs. 9	6 vs. 7	2 vs. 3	5 vs. 8	2 vs. 6	2 vs. 6	3 vs. 7	3 vs. 7	2 vs. 6
5 vs. 8	2 vs. 3	5 vs. 8	7 vs. 9	7 vs. 9	2 vs. 8	6 vs. 7	3 vs. 9	5 vs. 8	6 vs. 7	6 vs. 7
3 vs. 7	7 vs. 9	3 vs. 7	2 vs. 3	6 vs. 7	2 vs. 3	3 vs. 7	6 vs. 7	8 vs. 9	2 vs. 6	2 vs. 3
2 vs. 9	3 vs. 7	1 vs. 2	3 vs. 7	2 vs. 8	3 vs. 9	2 vs. 3	2 vs. 3	2 vs. 8	3 vs. 9	3 vs. 7
8 vs. 9	6 vs. 7	2 vs. 3	8 vs. 9	1 vs. 2	7 vs. 9	3 vs. 9	3 vs. 7	6 vs. 7	2 vs. 3	3 vs. 5
2 vs. 3	3 vs. 9	8 vs. 9	2 vs. 9	3 vs. 7	3 vs. 7	1 vs. 5	1 vs. 5	1 vs. 5	8 vs. 9	7 vs. 8
3 vs. 9	8 vs. 9	2 vs. 8	2 vs. 8	1 vs. 5	5 vs. 6	2 vs. 9	2 vs. 9	1 vs. 9	1 vs. 2	1 vs. 2
1 vs. 5	1 vs. 5	7 vs. 9	1 vs. 5	2 vs. 9	6 vs. 7	1 vs. 2	1 vs. 2	1 vs. 2	1 vs. 5	1 vs. 5
2 vs. 8	1 vs. 2	1 vs. 5	5 vs. 6	8 vs. 9	1 vs. 5	8 vs. 9	8 vs. 9	7 vs. 9	2 vs. 9	8 vs. 9
1 vs. 2	2 vs. 8	6 vs. 7	7 vs. 8	5 vs. 6	8 vs. 9	2 vs. 8	2 vs. 8	5 vs. 6	7 vs. 8	3 vs. 9
7 vs. 8	1 vs. 9	1 vs. 9	1 vs. 2	3 vs. 9	2 vs. 9	5 vs. 6	5 vs. 6	2 vs. 9	3 vs. 5	2 vs. 8
2 vs. 7	5 vs. 6	5 vs. 6	2 vs. 7	7 vs. 8	1 vs. 9	1 vs. 9	1 vs. 9	3 vs. 9	5 vs. 6	2 vs. 9
1 vs. 9	7 vs. 8	7 vs. 8	3 vs. 9	1 vs. 9	3 vs. 5	3 vs. 5	7 vs. 8	4 vs. 5	2 vs. 8	1 vs. 4
5 vs. 6	2 vs. 7	3 vs. 5	1 vs. 9	3 vs. 5	7 vs. 8	7 vs. 8	3 vs. 5	3 vs. 5	1 vs. 9	5 vs. 6
1 vs. 7	1 vs. 7	1 vs. 7	3 vs. 5	2 vs. 7	5 vs. 9	2 vs. 7	5 vs. 9	7 vs. 8	4 vs. 5	3 vs. 4
4 vs. 5	3 vs. 5	2 vs. 7	4 vs. 5	1 vs. 7	5 vs. 7	5 vs. 9	2 vs. 7	5 vs. 9	1 vs. 4	2 vs. 7
3 vs. 5	4 vs. 5	5 vs. 9	1 vs. 7	5 vs. 9	1 vs. 7	1 vs. 7	1 vs. 7	1 vs. 4	4 vs. 8	5 vs. 9
5 vs. 9	5 vs. 9	4 vs. 5	5 vs. 9	5 vs. 7	2 vs. 7	5 vs. 7	5 vs. 7	1 vs. 7	5 vs. 9	4 vs. 5
5 vs. 7	5 vs. 7	5 vs. 7	5 vs. 7	4 vs. 5	2 vs. 5	4 vs. 5	4 vs. 5	4 vs. 8	1 vs. 7	1 vs. 9
4 vs. 8	4 vs. 8	4 vs. 8	2 vs. 5	2 vs. 5	1 vs. 4	4 vs. 8	4 vs. 8	4 vs. 6	5 vs. 7	1 vs. 7
2 vs. 5	2 vs. 5	1 vs. 4	4 vs. 8	4 vs. 8	4 vs. 8	1 vs. 4	1 vs. 4	2 vs. 7	2 vs. 7	5 vs. 7
1 vs. 4	1 vs. 4	2 vs. 5	1 vs. 4	1 vs. 4	4 vs. 5	2 vs. 5	2 vs. 5	2 vs. 5	4 vs. 6	4 vs. 8
4 vs. 6	4 vs. 6	4 vs. 6	4 vs. 6	4 vs. 6	2 vs. 4	4 vs. 6	4 vs. 6	4 vs. 9	2 vs. 5	2 vs. 5
4 vs. 9	4 vs. 9	2 vs. 4	4 vs. 9	2 vs. 4	4 vs. 6	4 vs. 9	2 vs. 4	5 vs. 7	3 vs. 4	2 vs. 4
2 vs. 4	2 vs. 4	4 vs. 9	2 vs. 4	4 vs. 9	4 vs. 9	2 vs. 4	4 vs. 9	3 vs. 4	2 vs. 4	4 vs. 6
3 vs. 4	3 vs. 4	3 vs. 4	3 vs. 4	3 vs. 4	3 vs. 4	3 vs. 4	3 vs. 4	4 vs. 7	4 vs. 9	4 vs. 9
4 vs. 7	4 vs. 7	4 vs. 7	4 vs. 7	4 vs. 7	4 vs. 7	4 vs. 7	4 vs. 7	2 vs. 4	4 vs. 7	4 vs. 7

**Table 2.** Best to worst matches. Matches are listed from the best match (top row for each metric) to the worst match (bottom row for each metric).